Received: 26 July 2022 | Revised: 25 August 2022 | Accepted: 11 September 2022

DOI: 10.1111/jace.18811

Journal of the American Ceramic Society

RESEARCH ARTICLE

Unraveling the role of shell thickness and pore size on the mechanical properties of ceramic-based macroporous structures

Alberto Gomez-Gomez[1] | **Benedikt Winhard**[1] | **Erica Lilleodden**[1] | **Norbert Huber**[2,3] | **Kaline P. Furlan**[1]

[1]Hamburg University of Technology, Institute of Advanced Ceramics, Integrated Materials Systems Group, Hamburg, Germany

[2]Helmholtz-Zentrum Hereon, Institute of Materials Mechanics, Geesthacht, Germany

[3]Hamburg University of Technology, Institute of Materials Physics and Technology, Hamburg, Germany

Correspondence
Kaline P. Furlan, Hamburg University of Technology, Institute of Advanced Ceramics, Integrated Materials Systems Group, Denickestraße 15, 21073 Hamburg, Germany.
Email: kaline.furlan@tuhh.de

Funding information
Deutsche Forschungsgemeinschaft (DFG, German Research Foundation) – Projektnummer, Grant/Award Number: 192346071

Abstract

Macroporous structures are of interest for several technological applications such as catalysis, sensors, filters, membranes, batteries, energy conversion devices, structural colors, and reflective thermal barrier coatings. Ceramic-based inverse opal macroporous structures are especially interesting for high-temperature applications. However, the interrelation between the structural parameters, mechanical properties, and thermal stability of such structures is not yet clarified. In this work, we analyzed the mechanical properties as well as the thermal stability of aluminum oxide inverse opal three-dimensional macroporous structures with different macropore sizes and shell thicknesses produced by atomic layer deposition. Our results show that the structures' thermal stability increased with increasing shell thickness and macropore size, however, their higher stability was not linked to their mechanical properties. To be able to explain this unexpected behavior, finite element modeling simulations were performed, showing that bending stresses became more pronounced with increasing shell thickness, potentially creating additional critical sites for crack initiation and consequent structural failure.

KEYWORDS
atomic layer deposition, ceramics, macroporous structures, mechanical metamaterial

1 | INTRODUCTION

Inverse opals are a class of macroporous materials, which are lightweight, have low thermal conductivity, high surface area, and high permeability.[1–4] Their highly-periodical structure is comprised of repeating units in the order of a hundred nanometers up to microns, capable of controlling not only the electromagnetic radiation propagation,[5] but also the mass transport of species through its macropores, and depending on the fabrication process, mesopores and nanopores.[4] Moreover, the internal surfaces can be coated or functionalized to tune the surface interactions.[6] Hence, these materials are interesting for several technological applications such as catalysts, catalyst supports,

bioreactors, membranes, sensors, batteries, thermal insulators, bone grafting, energy conversion devices, and reflective thermal barrier coatings.[7–15]

The fabrication processes of inverse opals or more generally, macroporous three-dimensional (3D) structures, usually involve the infiltration of templates, referred to as colloidal crystals. The most common methods are based on sol-gel, including co-assembly[16] or colloid infiltration,[17,18] but there has been an increase in recent years of the usage of chemical vapor deposition[19] or atomic layer deposition (ALD).[20] A large variety of materials can be produced via ALD such as selenides, tellurides, sulfides, nitrides, metals, and oxides.[21] However, for successful coating and fabrication of inverse opal macroporous structures, it is necessary to assure no reaction between precursors and templates, and, in the case of polymeric-based templates, develop low-temperature cycles.[22] Moreover, polymeric templates can be oxidized during oxidant exposure[23,24] and already-established cycle parameters may not be suitable due to different growth mechanisms.[25] Despite its challenges, ALD presents several advantages such as surface-limited reactions, excellent thickness control, the capability of coating high-aspect-ratio templates, and the opportunity to produce tailor-made atomically mixed compounds.

Whilst most of the research efforts have been focused on polymeric and SiO_2 inverse opals, investigations have also been performed on metallic,[26,27] carbon-based,[28] silicon-based,[29] and ceramic inverse opals.[20,22,30–35] A variety of ceramic-based inverse opal macroporous structures have been reported such as silica,[17,36,37] silicon carbide,[38] titania,[20,39,40] alumina,[35,41,42] zirconia,[40] yttria-stabilized zirconia[18] and mullite.[22] When compared to metals and polymers, ceramics generally present a higher chemical, microbiological and thermal stability.[13] They are, however, less compliant and may fracture catastrophically under stress. Nonetheless, even though ceramic macroporous structures are usually more thermally stable than metallic and polymeric structures, especially when exposed to an air environment, they also undergo structural changes such as shrinkage[22] and extensive grain growth[35] when exposed to high temperatures (>1000°C). These become more critical at smaller length scales, such as the high-surface-area structures with nanometric features. Moreover, these morphological changes have a direct impact on the macropores structures' properties, thus may hinder their final function. We have been developing ceramic-based macroporous structures for high-temperature photonic applications,[18,20,22,35,43] which are capable of reflecting thermal radiation whilst also reducing the heat conduction by its highly-porous structures. It is a challenge, however, to keep the three-dimensional ordered structure stable at high temperatures (>1000°C) and yet functional. Such a challenge can be targeted by tailoring the chemical composition of the ALD shell, that is, the shell material, as demonstrated in one of our earlier publications,[22] or by focusing on optimization of the 3D structure features while keeping the shell material fixed. This work focuses on the latter approach.

Besides keeping their structure stable after exposure to high temperatures, these 3D structures should also exhibit sufficient mechanical properties to allow their handling, mounting, and application. The size effect of these structures, often in the micrometer and nanometer scale, opens up the opportunity for further increase in their mechanical properties, the so-called mechanical metamaterials. Inverse opal structures have been shown to outperform most of the state-of-the-art techniques to produce high-performance mechanical metamaterials, being surpassed only by glassy nanolattices.[44] The mechanical properties of co-assembled SiO_2 inverse opals further reinforced with TiO_2 via ALD have been investigated in former works.[17,37] The increase in the coating thickness, that is, shell and struts thicknesses, led to a direct increase in both strength and moduli, achieving specific strengths as high as 460 MPa/(mg/m^3) for structures with macropores size of around 756 nm. This was also observed for alumina inverse opals,[45] although in this work the macropore size was almost 3 times smaller, corresponding to around 260 nm. Metallic inverse opal structures with specific strengths up to 230 MPa/(mg/m^3) were reported by Pikul et al.[26] Interestingly, the structures presented an increase in their strut yield strength when the strut diameter was decreased, varied by varying the template particle size. In this work, we have investigated the influence of modifications in structural parameters, namely ALD shell size and macropore size (Figure 1), on the thermal stability and mechanical properties of inverse opal ceramic-based macroporous structures.[1]

2 | MATERIALS AND METHODS

2.1 | Vertical convective self-assembly

Colloidal crystals of monodisperse polystyrene (PS) particles (microparticles GmbH) were fabricated by vertical convective self-assembly onto sapphire substrates (< 1–102 >, Crystec GmbH) inside a humidity chamber (Memmert HCP 108), at 70% RH and 55°C for 96–120 h depending on the substrate total area, 400 or 750 cm^2, respectively. The PS particles suspensions were diluted with deionized filtered water inside polytetrafluoroethylene beakers, and were comprised of three different particles sizes: 0.52 ± 0.01 μm (1.0 mg/ml), 0.75 ± 0.02 μm (0.8 mg/ml), and 1.04 ± 0.04 μm (0.9 mg/ml). Prior to self-assembly the substrates were

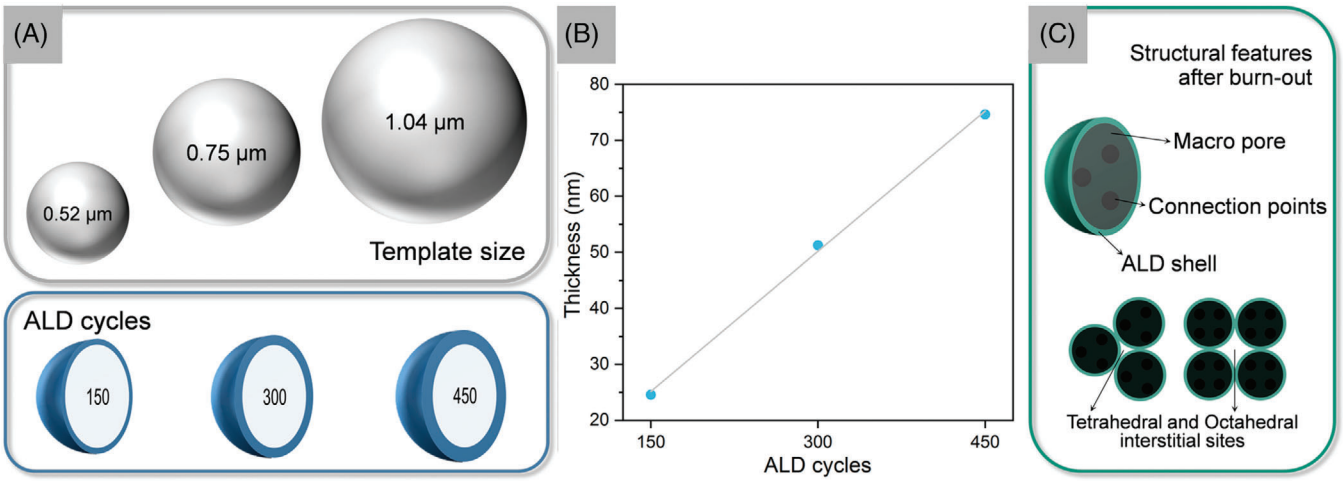

FIGURE 1 Schematic drawing of samples analyzed in this study, in which the (A) template size and atomic layer deposition (ALD) cycles number were varied. (C) The structural features of the 3D macroporous ceramics (inverse opals) after burn-out are directly dependent on these parameters. Macropore size is defined by the template, while the shell thickness depends on the number of ALD cycles, as shown in (B). Connection points and nodes sizes are defined by both the template and ALD cycles

cleaned by 1 h sonication in a detergent solution (Mucasol 1%, Brand, Merz Hygiene GmbH), brushed, rinsed, and dried with filtered nitrogen. Furthermore, oxygen plasma was applied to sapphire substrates for 20 min right before immersion, as an extra cleaning step plus surface activation.

2.2 | Atomic layer deposition

The PS templates produced by vertical convective self-assembly were coated by low-temperature ALD of aluminum oxide in a home-made reactor (Hamburg University of Technology, Institute of Advanced Ceramics), using trimethylaluminium (TMA; Strem chemicals) and deionized water (diH_2O) as reactants. To homogeneously infiltrate the whole template, a full exposure mode with a constant purge flow of nitrogen (30 sccm) was used. The reactants TMA and diH_2O were alternated with 0.1/20/90 and 0.2/20/90 s of pulse, exposure, and pump times, respectively. The low temperature of the process (95°C) was required to avoid surpassing the PS glass transition temperature and thus prevent any possible damage to the template. After the ALD process, the PS template was burned out in a Muffle furnace in air (0.3°C/min, 500°C, 30 min), leading to the macroporous ceramic structures (inverse opals). In such structures, the original PS size corresponds to the so-called macropore size, while the shell thickness, that is, ALD coating thickness was varied by increasing the number of cycles during the ALD process. An overview of the samples produced can be visualized in Figure 1. The shell thickness monitoring was performed by spectroscopic ellipsometry with an incident angle of 70° (SENPro; SENTECH Instruments GmbH), by which the thickness and refractive index of films deposited onto standard silicon wafers (as received, <100>, a native oxide layer, Si-Mat Silicon Materials) placed near the samples during the cycles was measured. The resulting thicknesses (Figure 1B) were in good agreement with the expectations based on the estimated growth per cycle of films infiltrated/deposited onto PS beads templates.[35] An average growth rate of 1.66 ± 0.06 Å/cycle and a refractive index value of $n = 1.65 \pm 0.03$ (@632.8 nm) were achieved, respectively.

2.3 | Thermal processing and characterization

The ceramic-based inverse opals were heat treated in air in a tubular furnace with a 5°C/min heating rate up to the heat treatment temperatures of 1200 and 1400°C, where the samples were kept for 1 and 4 h, respectively. Their structural morphology was analyzed by scanning electron microscopy (SEM; Zeiss Supra 55 VP) prior to and after each heat treatment. A low voltage of 2 kV was used to avoid sample charging and the work distance was set to 5–6 mm for all samples.

For the characterization of the mechanical properties, nanoindentation tests were carried out (G200 nanoindenter; formerly Agilent, now KLA Tencor, CA, USA) using a flat-punch with 10 μm of diameter (Synton MDP, Port, Switzerland) and a fixed displacement rate of 10 nm/s up to 2000 nm of penetration depth. The tests were performed under continuous stiffness measurement mode, with an oscillation amplitude of 2 nm at a frequency of 45 Hz.

The elastic modulus (E) was estimated using the harmonic contact stiffness data recorded in the loading part of the strain-displacement curve. The mean values of E presented in this work were calculated from the plateau values, that is, once the stiffness has stabilized before the first failure event was recorded. For simplicity, the influence of the elastic displacement of the sapphire substrate is neglected since its stiffness is one order of magnitude greater than the structures analyzed. At least 4 indents were performed on each sample.

3 | RESULTS AND DISCUSSION

3.1 | Macroporous ceramics structural evolution

The difference in the morphology of the macroporous ceramics with different structural features is noticeable, especially regarding the ALD cycles (Figure 2), which define the shell size (Figure 1). The spacing between the spherical shells and the interstitial site size (hereafter referred to as nanopores) is reduced when the shell thickness is increased (compare Figure 2D,E), which was expected. For a certain template size, the initial connection points between the template particles have the same size and since the ALD coating is based on surface reactions, the coating will mimic the template structure up to its filling limit, that is, the connection points size will be the same for a certain template size, but not the nanopores. When the structures are produced via sol-gel these sites are filled and referred to as nodes. In the case of ALD-based structures such as the ones in this work, there is a limit for which the precursors can reach these nanopores, and thereby, the precursors' access points to these sites shall be eventually closed and the nanopore will remain within the structure.[46] The geometrical theoretical filling limit for an ALD coating into <111> planes of a self-assembled Face-Centered cubic (FCC) structure is estimated to be 7.75% of the template diameter[47] and thereby, the ALD coating thickness limit is estimated to be 40, 60, and 80 nm for template diameters of 0.52, 0.75, and 1.04 μm, respectively. While the nanopores formed at the interstitial sites will remain as pores, the rest of the structure can be further coated, increasing its shell's thickness. Moreover, the overall packing fraction of the template particles is known to be lower than 74% due to the presence of common self-assembly defects[22,48,49] and that the connection points could have their size increased due to a "sintering" of the PS template[26] during the 2 h pre-vacuum time performed prior to the ALD process, both resulting in a template structure with higher porous fraction available for infiltration. As a matter of fact, there have been earlier reports of higher filling fractions[47,50] up to 95%, in which a 70 nm ALD-ZnS coating was deposited onto a 300 nm diameter template[50] or a 34 nm ALD-TiO_2 film was deposited onto a 266 nm template.[47] We also observed higher filling fractions than the theoretical limit value for all the template sizes without the occurrence of an overlayer (see Figure S1). It is important to mention that for the samples with 0.52 and 0.75 μm of template size we have observed, however, the occurrence of some small satellites' growth for the ALD process with 450 cycles (Figure 2C).

These structural differences are relevant for the thermal stability after exposure at 1200°C for 1 h (Figure 3). The thinner shells corresponding to 150 ALD cycles already show signs of degradation with a random network of cracks for all studied template sizes, although the cracks in the samples with a template size of 1.04 μm are clearly smaller and less connected than for the samples produced with 0.52 and 0.75 μm template sizes. Cracks are also observed for samples produced with 300 ALD cycles, while no clear cracks are identified for the 450 ALD cycles' samples, but lines are visible in the shells' surface, either as pre-cracks or grain sizes due to the alumina phase transformation. Before 1200°C, the aluminum oxide shells undergo at least 3 phase transformations and consist only of alpha-alumina, after the heat treatment at 1200°C, as demonstrated in a previous study.[35]

After further exposure at 1400°C for 4 h (Figure 4 and Figure S2) all the samples with 150 and 300 ALD cycles are completely distorted and a vermicular structure is clearly visible for the samples with 1.04 μm template size, as well as for the samples with 0.75 μm template size and the thinner shell (150 ALD cycles). Such vermicular structures are well-known and frequently reported for aluminum oxide materials.[7,8,10,13–15,51–54] However, in such macroporous structures, they seem to be more stable than in sol-gel[54] or inkjet printed[13] structures, and are not altered with increasing sintering time, discussed in detail elsewhere.[35] Classical sintering theory[55] predicts that such highly curved interfaces should be smoothed or reduced and such an open filter-like network with large domains is not expected. Moreover, instead of expected neck growth and porosity reduction, as observed in classic bulk-particle solid-state sintering, the sintering of the shells results in the enlargement of the connection points (Figure 5A) and grain growth. Nonetheless, it is possible to find some resemblance to the simple two-particle model for sintering, even though in the inverse opals case only the shells are available for sintering (Figure 5B).

While for thinner shells (150 cycles, Figure 4A–C) the template size does not influence the resulting structure after temperature exposure, for thicker shells the heat-treated structure differs depending on the template size. Oblate-like structures are formed for the samples

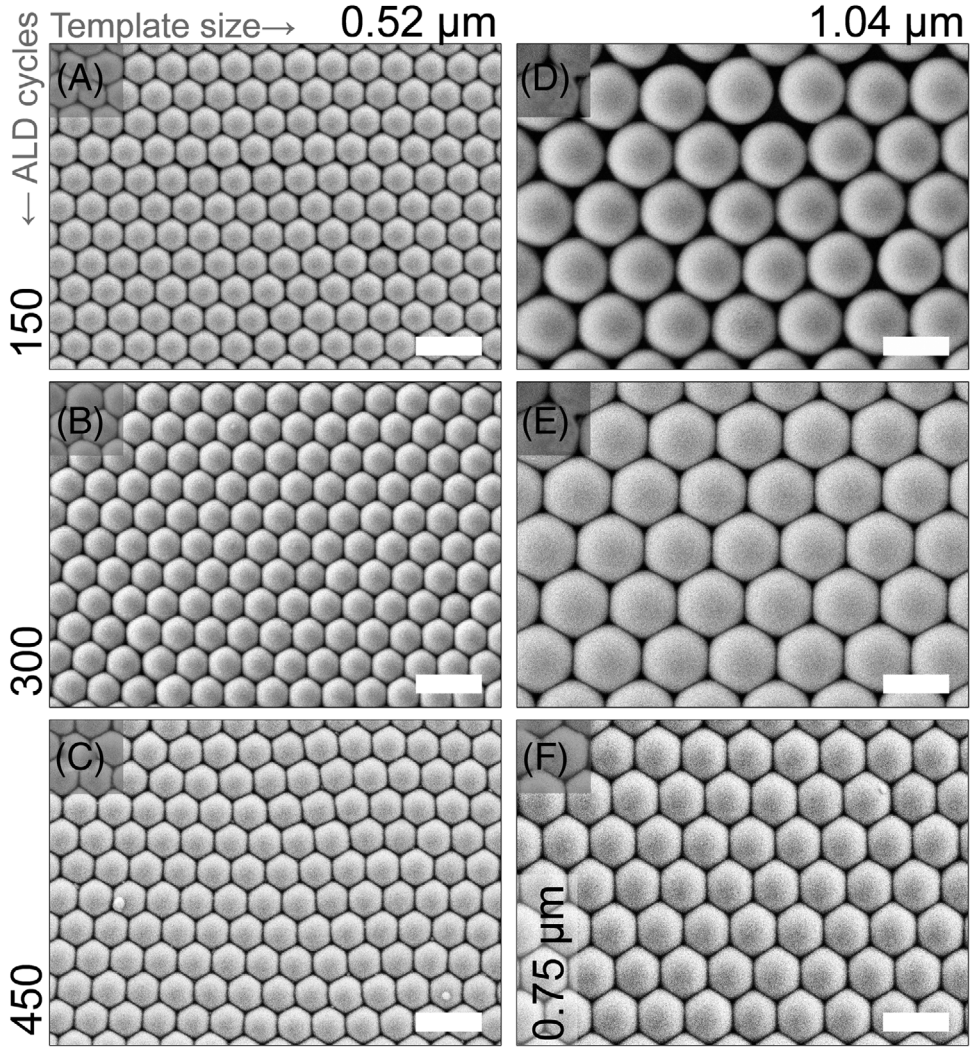

FIGURE 2 Top view of different structures of aluminum oxide inverse opals according to the template sizes (A–C) 0.52 μm, (D–E) 1.04 μm, (F) 0.75, and the number of atomic layer deposition (ALD) cycles (A, D) 150 (B, E) 300 (C, F) 450. Imaged by scanning electron microscopy (SEM) after template burn-out; top view. Scale bars represent 1 μm

produced with 0.52 μm template size and 300 and 450 ALD cycles, as well as the ones with 0.75 μm and 300 ALD cycles (Figure 4D,G,E, respectively). Meanwhile, the samples produced with thicker shell (450 cycles) for both 0.75 and 1.04 μm template size retain their 3D macroporous structure after thermal exposure. Such structures also are stable in the cross section (Figure 6A–C), whereas a closer look at the sample produced with a 0.52 μm template size shows signs of deformation (top corner of Figure 6A). The filter-like and oblate-like structures exemplified by Figure 6D,E, respectively, are also present in the samples' whole thickness.

All the aluminum oxide macroporous structures here presented are amorphous after deposition and crystallize upon heating.[35] Still, nucleation and growth of crystallites cannot take place in areas smaller than the critical nuclei radius,[56] which could be the case for the thinner shells. Thereby, one can attribute possibly different crystallites density per volume depending on the shell thickness, that is, thicker shells will present, on average, more crystallites than thinner shells. The crystallites form grains in the material and a single grain can consist of one (single crystal) or more crystallites, which will sinter upon thermal exposure.

In polycrystalline ceramic materials, solid-state sintering is defined by diffusion. While grain boundary diffusion and lattice diffusion from the grain boundary contribute to densification, surface diffusion and lattice diffusion from the surface do not.[57] The 3D macroporous structures studied here have a very high surface-to-volume ratio, thereby, the occurrence of surface diffusion may be more relevant to such structures when in comparison to bulk samples. Moreover, the existence of macropores leads to a restriction of sintering to the shell area, as it is not possible

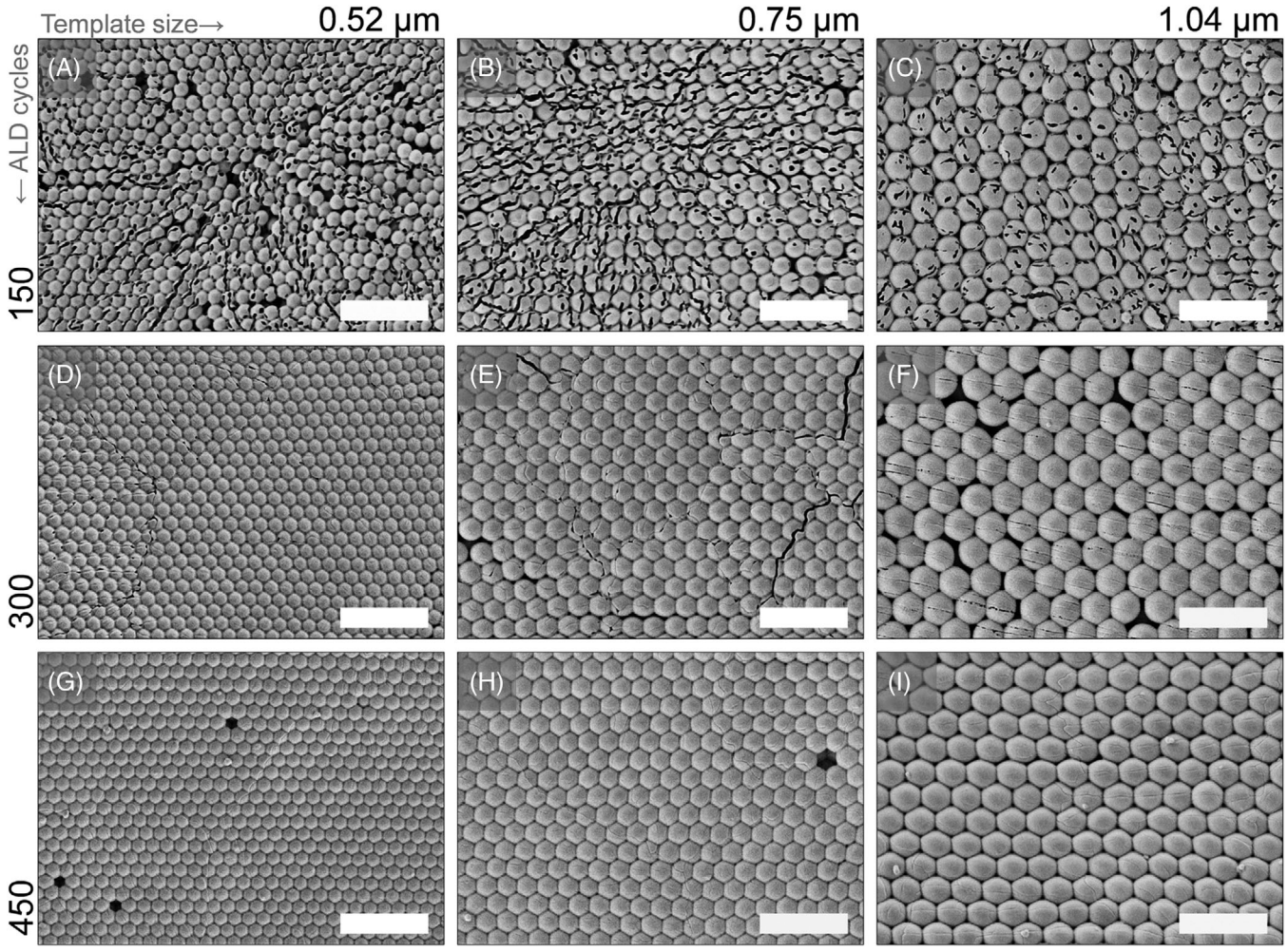

FIGURE 3 Comparison between the top view morphology of inverse opals imaged by scanning electron microscopy (SEM) after the heat treatment performed at 1200°C for 1 h. Template size is 0.52, 0.75, and 1.04 μm for (A, D, G), (B, E, H), and (C, F, I), respectively. The number of atomic layer deposition (ALD) cycles is (A–C) 150, (D–F) 300, and (G–I) 450. Scale bars correspond to 3 μm

for atoms from one side of the shell to just "jump" to the other side of the shell, crossing the macropores. This inhibition contributes to the formation of the vermicular, filter-like structure. Smaller templates and thinner shells have a higher ratio of surface per volume of shell material, so one could infer that the surface diffusion per volume diffusion ratio is greater in these cases, leading to no densification, that is, filter-like structures. No matter the shell thickness, the samples fabricated with 0.52 μm template size presented less stability than 0.75 and 1.04 μm. Besides having more surface area, these samples also present a larger number of connection points per volume. Moreover, the curvature of the shells for the samples produced with the 0.52 μm template is bigger than for the bigger ones (Figure 7B). For solid particles and solid-state sintering, the diffusion of atoms occurs in the direction of lower partial pressure areas. For our case, this corresponds to the points where the curvature is bigger, that is, the intersecting points between shells (see Figure 7). The higher the curvature is, the higher the driving force for the transport of matter and thus, sintering. In the case of the macroporous structures studied here, thinner shells present a higher curvature radius at the perimeter of the intersecting points between shells than thicker shells, considering a case where the template size is the same (Figure 7C), which explains why the samples produced with smaller template sizes and thinner shells are less stable.

The formation of oblate-like structures (Figure 4D,E,G) is hypothesized to be related to grain growth occurring at a stage in which the structure is not yet fully distorted. This is in part related to the above-mentioned points. As explained, the driving force for sintering is larger as the smaller the template size and the thinner the shell is. Thereby, taking the 0.52 μm case as an example and 1400°C as the sintering temperature, the thinner shell structure already experienced larger sintering and it is fully distorted, thus, grain growth can only occur in the z-direction

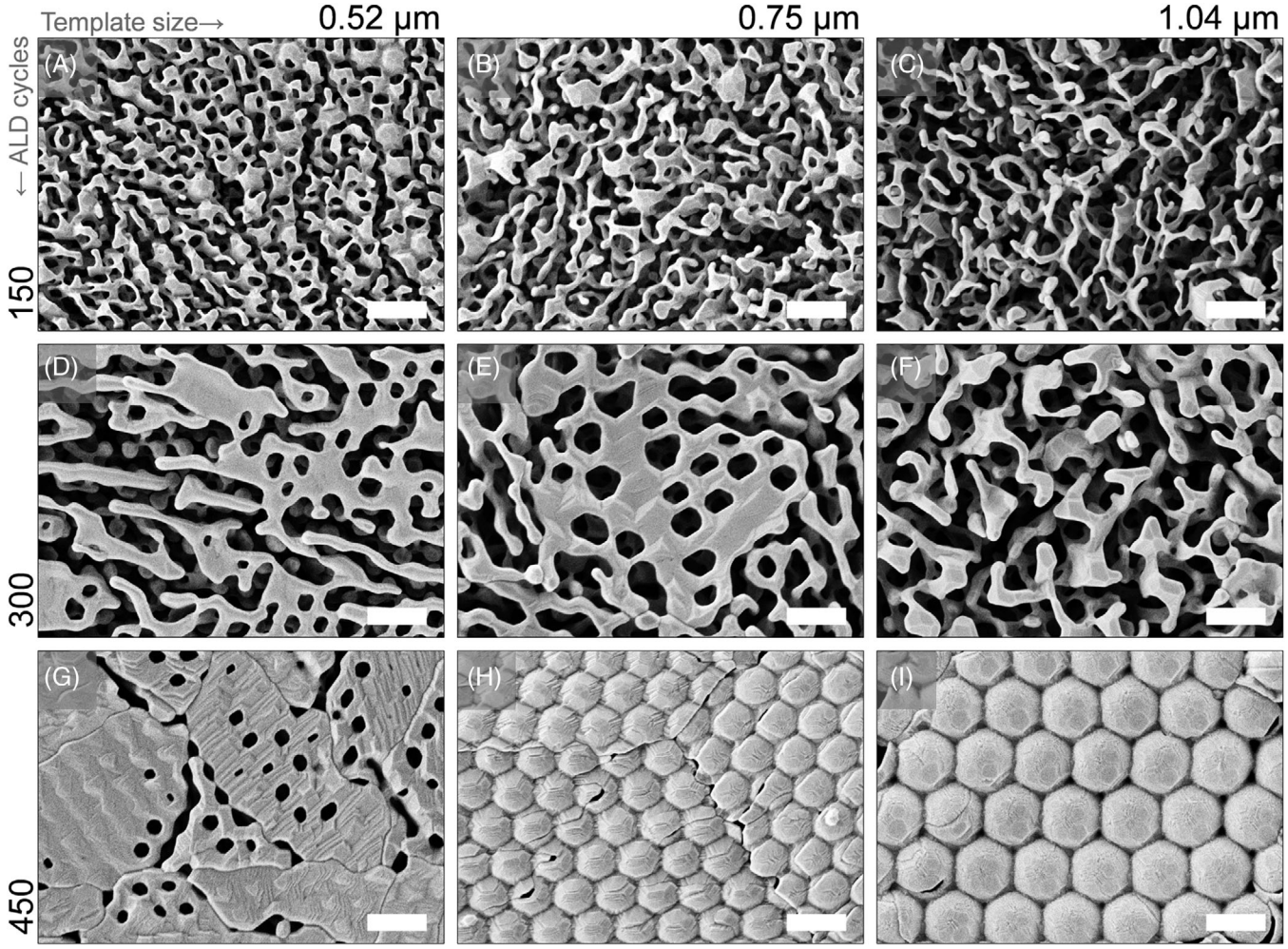

FIGURE 4 Comparison between the top view morphology of aluminum oxide macroporous structures imaged by scanning electron microscopy (SEM) after heat treatment performed at 1400°C for 4 h. Template size is 0.52, 0.75, and 1.04 μm for (A, D, G), (B, E, H) and (C, f, i), respectively. The number of atomic layer deposition (ALD) cycles is (A–C) 150, (D–F) 300, and (G–I) 450. Scale bars correspond to 1 μm

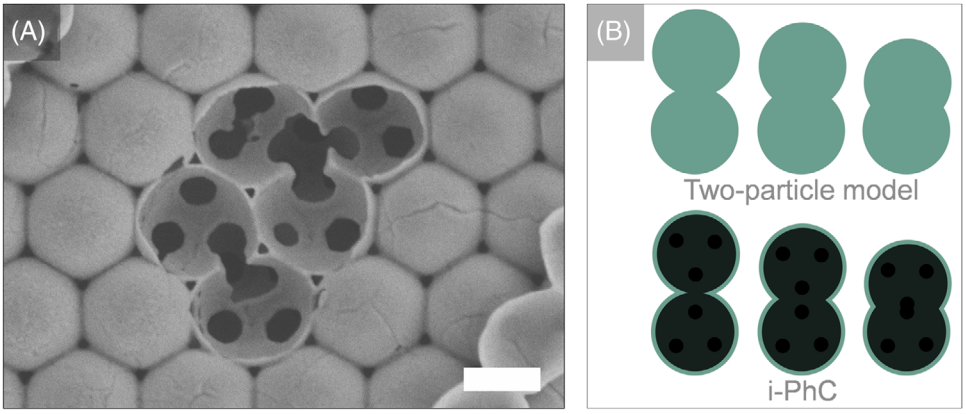

FIGURE 5 (A) Top-view scanning electron microscopy (SEM) image of an alumina macroporous structure fabricated with 0.75 μm template and 450 atomic layer deposition (ALD) cycles after heat treatment at 1200°C for 1 h showing the enlargement and joining of connection points. The scale bar is 500 nm. (B) Schematic drawing of the two-particle sintering model and a representation of shells sintering in the macroporous structures (inverse opals, also called -i-PhC)

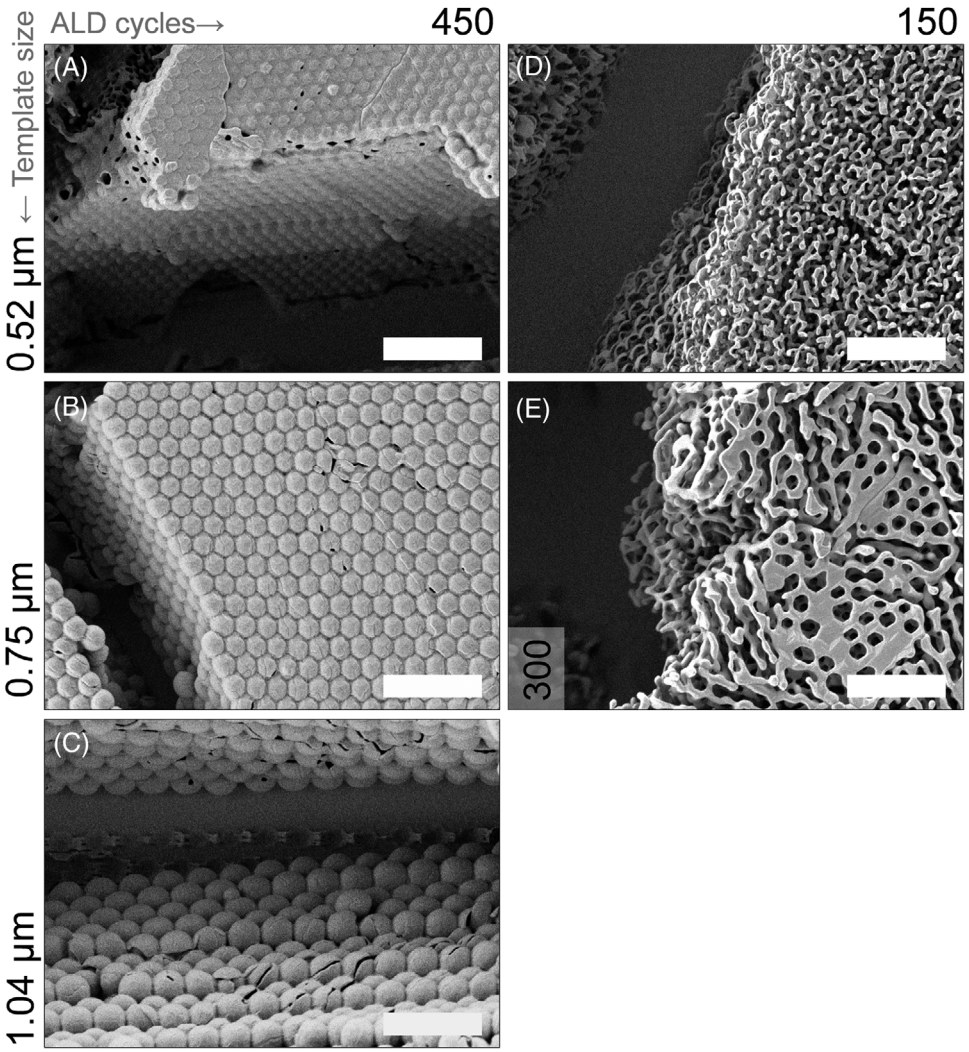

FIGURE 6 Inclined view of the morphology of the aluminum oxide macroporous structures in scanning electron microscopy (SEM) after heat treatment performed at 1200°C for 1 h. Template size and atomic layer deposition (ALD) cycle information are indicated on the labels within the image. Scale bars correspond to 3 μm

of the vermicular grains as there is little or no contact between the shells at the top layer anymore. On the other hand, structures that still present the top shells will experience grain growth also at these spots, in the x and y direction. Note in Figure 4G that the middle left grain still shows a resemblance to the top shell shape, although it is massive (bigger than 3×3 μm).

3.2 | Mechanical properties

Nano-indentation tests were performed to analyze the impact of the structural parameters on their mechanical properties, particularly on compression strength and elastic modulus, σ_{max} and E, respectively. Typical stress-strain curves and associated elastic moduli can be visualized in the supplementary information (Figure S3). The results showed that a decrease in the template size, thus the macropore size, enhances both σ_{max} and E (Figure 8). This was expected, because for a given number of ALD cycles, the shell thickness is constant and, therefore, the solid fraction increases with decreasing template size. This relationship is especially clear in the samples with the thinnest shell (150 ALD cycles). However, the influence of the macropore size on the mechanical properties seems to have a saturation limit as the shell of the macroporous structures thickens. Thereby, all the structures with thicker shell sizes (450 ALD cycles) present values that are equal to or lower than the samples produced with 300 ALD cycles. A possible explanation will be given with help of finite element simulations, below.

Nonetheless, the elastic moduli raised from twofold to threefold when comparing the samples with thinner shells (150 ALD cycles) to those with the same macropore size

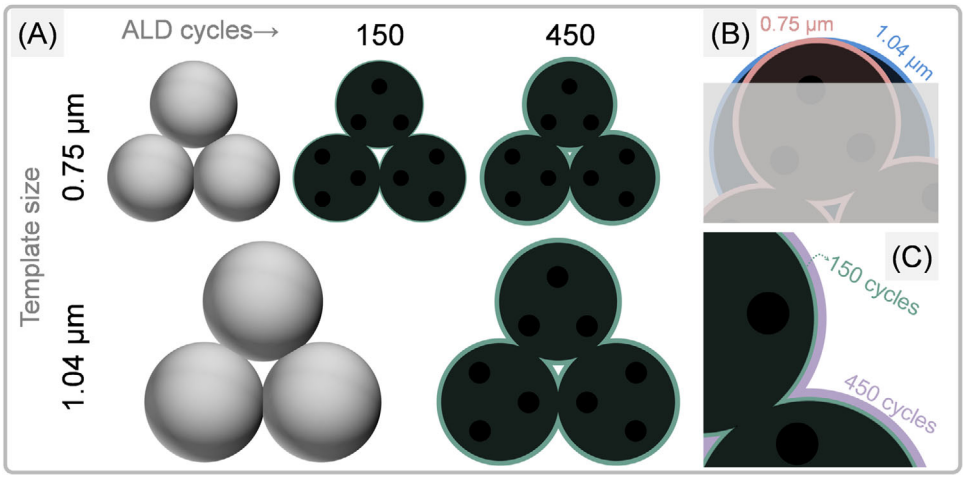

FIGURE 7 Schematic drawing of the colloidal templates and the ceramic macroporous structures (inverse opals) and their structural features. Thinner shells and smaller templates lead to smaller nanopores as demonstrated in (A). For a fixed shell thickness (number of atomic layer deposition [ALD] cycles) the curvature is bigger for smaller templates, shown in (B). The grey box is just a guide to the eye. An increase in the shell thickness, for the same template size, leads to a reduction in the curvature at the intersecting points between the shells shown in (C)

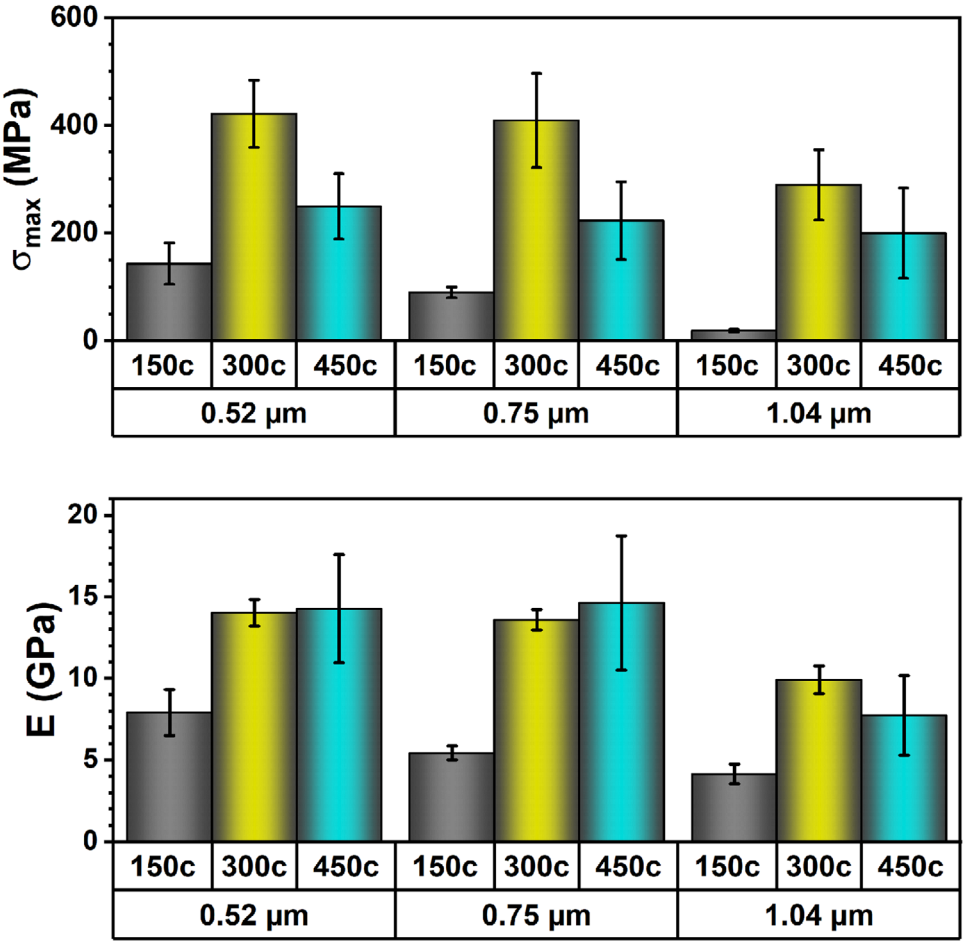

FIGURE 8 Mechanical properties of aluminum oxide inverse opal macroporous structures according to template size and number of atomic layer deposition (ALD) cycles: (A) yield strength (B) elastic moduli

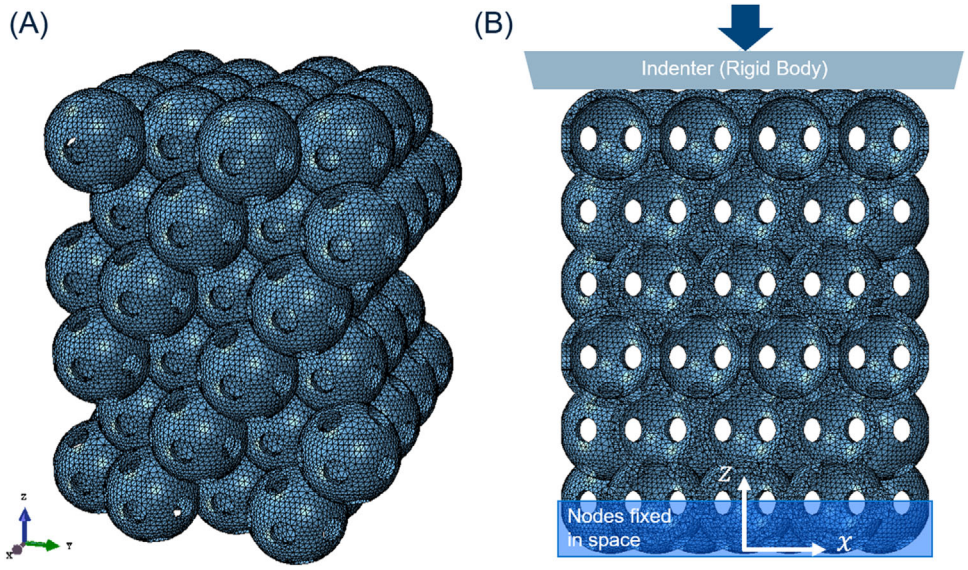

FIGURE 9 Example of a finite element mesh for template size of 0.75 μm and 450 atomic layer deposition (ALD) cycles, corresponding to a thickness of 75 nm. The perspective view in (A) shows the closed shell on the top layer, which is contacted by the indenter, modeled as a rigid body, and schematically shown in the cut view (B)

but thicker shells (300 and 450 ALD cycles). While the elastic moduli were not greatly altered when comparing the samples produced with 300 or 450 ALD cycles, the compression strength values σ_{max} were consistently lower for thicker shells, independent of the macropore size. One possible reason is that the reduced strength of the samples with thicker shells (450 ALD cycles) is related either a greater number of defects (potential failure points) of the ceramic structures. Another reason could stem from a change in the failure mechanism or location, caused by the substantial increase of the shell thickness, which is investigated in the next section by using finite element simulations.

3.3 | Finite element simulations

The hypothesis of a possible change in the fracture mechanism can be addressed by finite element simulations. In total, nine models were created for all possible combinations of template sizes, D, and ALD coating thicknesses, t, as presented in Figures 9 and 11, respectively. Stacks of six layers of inverse opals were modeled in an fcc stacking, where the nodes of the lower half of the bottom layer are fixed in space, see Figure 9. For all simulations, performed with Abaqus,[58] Young's modulus and Poisson's ratio for the ALD shells were assumed with 175 GPa and 0.24, respectively.

The macroscopic Young's modulus, determined for a macroscopic strain of 5%, is shown in Figure 10 for three variations of the model setup. The results labeled

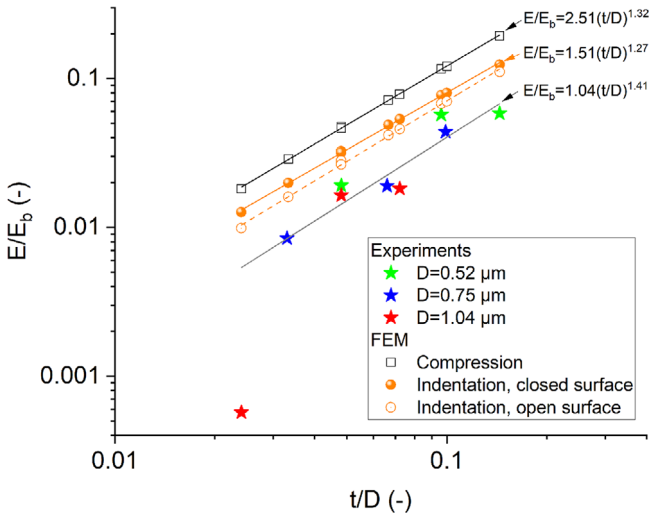

FIGURE 10 Comparison of macroscopic mechanical stiffness from FE simulations and experiments

"compression" were obtained by a displacement boundary condition applied to nodes in the top half layer, which gives the highest stiffness. Adding the indenter and a contact condition with the closed surface of the top layer of inverse opals leads to a drop in stiffness by about 40%. In comparison, for a top surface in which the connecting points are kept open, a comparably smaller effect in the macroscopic stiffness can be seen (open symbols, dashed line). Relative to the simulation results with indenter and contact, the experimental results are further reduced in stiffness by ~30%. This difference is due to the perfect order that is inherent in the simulation model along with rigid fixation

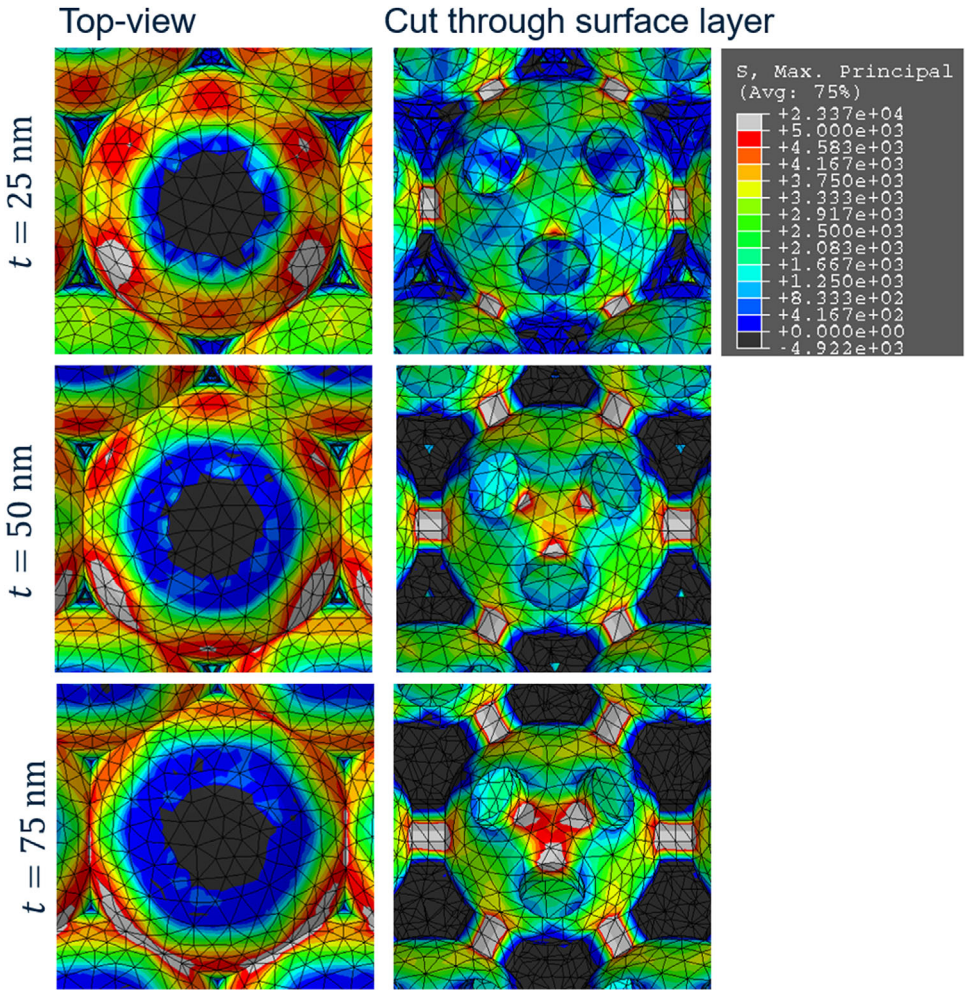

FIGURE 11 Local stress distribution under load for the template size D = 0.52 μm and varying atomic layer deposition (ALD) shell thickness from 25 nm (top row) to 75 nm (bottom row). The left column shows the top view of the surface in contact with the indenter, the right column shows the stress distribution inside the top-layer opal (cut through half of the top-layer of inverse opals)

of the bottom layer, whereas variations in template diameter and their arrangement as well as the contact with the substrate can be attributed to the 30% drop in the measured stiffness.

Overall, the dependence on the thickness to template size ratio t/D follows similar power-law relations with some variation in the exponent from ~1.3 (simulations) to ~1.4 (experiments), if the outlier for the lowest t/D ratio is ignored in the fit of the experimental data. From the agreement in the trends of stiffness versus thickness to template size ratio, it can be expected that the local stress distributions should be reasonable and can provide some helpful insights into possible changes in the fracture mechanism for an increasing shell thickness.

Figure 11 exemplarily shows the variation of the local stress distribution for the smallest template with D = 0.52 μm, which appears also to be the most sensitive case when the shell thickness is increased to the maximum thickness of 75 nm, see Figure 8. The shell thickness increases from the top to the bottom row of images shown in Figure 11, where the color scheme is the same for all images. Within the left row, showing the indented surface from the top, a stress concentration appears close to the triple points for the 50 nm shell thickness, which then moves to the connecting points for the 75 nm thickness. This is caused by the bending strain induced in the outer surface of the shell, along with the shorter lever length toward the connecting points. The relocation of this stress concentration might cause early fracture for the largest shell thickness because the stress concentration moves into the sharp notch that is formed in the vicinity of the connecting point.

Another potential spot for initiation of fracture can be found inside the inverse opals, visible in the right column of Figure 11. For the lowest shell thickness of 25 nm, the connecting points are causing the highest stresses, and fracture will likely be initiated in these places. However, for increasing shell thickness, a new stress concentration

emerges in the center of the shell of the inverse opal. For the largest shell thickness of 75 nm, it reaches a similar stress value to the connecting points visible in the cut plane. Therefore, it is possible that the fracture initiation site moves from the circumference for 25 and 50 nm shell thickness to the center bottom and top location at the inner surface for the largest shell thickness of 75 nm. This change in the stress distribution is also caused by bending stresses, which become increasingly important for thick shells. This is particularly the case for the top surface that undergoes flattening by the indentation contact, causing tensile stresses on the opposite side of the shell inside the inverse opal. Because thicker shells produce larger tensile stresses on the inside surfaces, the early fracture of the inverse opals with the thickest shells observed experimentally is reasonable. Furthermore, as can be seen from the evolution of the stress in Figure 11, right column, the number of critical locations is clearly increased for the largest shell thickness and, due to this, also the probability of failure.

4 | CONCLUSIONS

This work assessed the influence of structural parameters, namely macropore size, and shell thickness, on the thermal stability and mechanical properties of aluminum oxide inverse opal 3D macroporous structures produced by ALD. The results showed that the thermal stability of such structures is higher for thicker shells and larger macropores, while the mechanical properties followed no clear trend, rather peaking at the intermediate thickness and macropore size values. FEM simulations have shown that this unexpected behavior is likely caused by bending stresses that became more pronounced with increasing shell thickness, potentially creating new sites for crack initiation leading to mechanical failure upon crack propagation.

ACKNOWLEDGEMENT

Funded by the Deutsche Forschungsgemeinschaft (DFG, German Research Foundation) – Projektnummer 192346071 – SFB 986. We thank Dr. Robert Zierold and Prof. Robert Blick from the Center for Hybrid Nanostructures at the University of Hamburg for providing access to an Ellipsometer. We also acknowledge technical staff Lisa Fitzek for some of the image acquisition at the SEM and part of the colloidal crystals' assemblies.

Open access funding enabled and organized by Projekt DEAL.

CONFLICT OF INTEREST

The authors declare that they have no conflict of interest.

ORCID

Kaline P. Furlan https://orcid.org/0000-0003-4032-2795

REFERENCES

1. Phillips KR, England GT, Sunny S, Shirman E, Shirman T, Vogel N, et al. A colloidoscope of colloid-based porous materials and their uses. Chem Soc Rev. 2016, 45(2):281–322.
2. Stein A, Wilson BE, Rudisill SG. Design and functionality of colloidal-crystal-templated materials–chemical applications of inverse opals. Chem Soc Rev. 2013, 42(7):2763–803.
3. Ruckdeschel P, Philipp A, Retsch M. Understanding thermal insulation in porous, particulate materials. Adv Funct Mater. 2017, 27(38):1702256.
4. Yeo SJ, Choi GH, Yoo PJ. Multiscale-architectured functional membranes utilizing inverse opal structures. J Mater Chem A. 2017, 5:17111.
5. Lee HS, Kubrin R, Zierold R, Petrov AY, Nielsch K, Schneider GA, et al. Thermal radiation transmission and reflection properties of ceramic 3D photonic crystals. J Opt Soc Am B. 2012, 29(3):450.
6. Toivola Y, Stein A, Cook RF. Depth-sensing indentation response of ordered silica foam. J Mater Res. 2004, 19(1):260–71.
7. Liu R, Li Y, Wang C-A, Tie S. Fabrication of porous alumina–zirconia ceramics by gel-casting and infiltration methods. Mater Des. 2014, 63:1–5.
8. Montero M, Molina T, Szafran M, Moreno R, Nieto MI. Alumina porous nanomaterials obtained by colloidal processing using d-fructose as dispersant and porosity promoter. Ceram Int. 2012, 38(4):2779–84.
9. Tian F, Lyu J, Shi J, Tan F, Yang M. A polymeric microfluidic device integrated with nanoporous alumina membranes for simultaneous detection of multiple foodborne pathogens. Sens Actuators, B. 2016, 225:312–8.
10. Fang H, Gao JF, Wang HT, Chen CS. Hydrophobic porous alumina hollow fiber for water desalination via membrane distillation process. J Membr Sci. 2012, 403–404:41–6.
11. Li S-J, Xing Y, Tang M-Y, Wang L-H, Liu L. A novel nanomachined flow channel glucose sensor based on an alumina membrane. Anal Methods. 2013, 5(24):7022–9.
12. Di Costanzo T, Fomkin AA, Frappart C, Khodan AN, Kuznetsov DG, Mazerolles L, et al. New method of porous oxide synthesis: alumina and alumina based compounds. Mater Sci Forum. 2004, 453-454:315–22.
13. Chen Z, Brandon N. Inkjet printing and nanoindentation of porous alumina multilayers. Ceram Int. 2016, 42(7):8316–24.
14. Li S, Wang C-A, Zhou J. Effect of starch addition on microstructure and properties of highly porous alumina ceramics. Ceram Int. 2013, 39(8):8833–9.
15. Nagaoka T, Tsugoshi T, Hotta Y, Sato K, Watari K. Fabrication of porous alumina ceramics by new eco-friendly process. J Ceram Soc Jpn. 2005, 113(1313):87–91.
16. Hatton B, Mishchenko L, Davis S, Sandhage KH, Aizenberg J. Assembly of large-area, highly ordered, crack-free inverse opal films. Proc Natl Acad Sci U S A. 2010, 107(23):10354–9.

17. do Rosário JJ, Lilleodden ET, Waleczek M, Kubrin R, Petrov AY, Dyachenko PN, et al. Self-assembled ultra high strength, ultra stiff mechanical metamaterials based on inverse opals. Adv Eng Mater. 2015, 17(10):1420–4.
18. Kubrin R, do Rosario JJ, Lee HS, Mohanty S, Subrahmanyam RP, Smirnova I, et al. Vertical convective coassembly of refractory YSZ inverse opals from crystalline nanoparticles. ACS Appl Mater Interfaces. 2013, 5(24):13146–52.
19. Yates HM, Pemble ME, Blanco A, Míguez H, López C, Meseguer F. Growth of tin oxide in opal. Chem Vap Deposition. 2000, 6(6):283–5.
20. Pasquarelli RM, Lee HS, Kubrin R, Zierold R, Petrov AY, Nielsch K, et al. Enhanced structural and phase stability of titania inverse opals. J Eur Ceram Soc. 2015, 35(11):3103–9.
21. Miikkulainen V, Leskelä M, Ritala M, Puurunen RL. Crystallinity of inorganic films grown by atomic layer deposition: overview and general trends. J Appl Phys. 2013, 113(2):21301.
22. Furlan KP, Larsson E, Diaz A, Holler M, Krekeler T, Ritter M, et al. Photonic materials for high-temperature applications: synthesis and characterization by X-ray ptychographic tomography. Appl Mater Today. 2018, 13:359–69.
23. Steier L, Bellani S, Rojas HC, Pan L, Laitinen M, Sajavaara T, et al. Stabilizing organic photocathodes by low-temperature atomic layer deposition of TiO 2. Sustain Energy Fuels. 2017, 1(9):1915–20.
24. Bailey PS. The reactions of ozone with organic compounds. Chem Rev. 1958, 58(5):925–1010.
25. Guo HC, Ye E, Li Z, Han M-Y, Loh XJ. Recent progress of atomic layer deposition on polymeric materials. Mater Sci Eng C Mater Biol Appl. 2017, 70(Pt 2):1182–91.
26. Pikul JH, Özerinç S, Liu B, Zhang R, Braun PV, Deshpande VS, et al. High strength metallic wood from nanostructured nickel inverse opal materials. Sci Rep. 2019, 9(1):719.
27. Pikul JH, Dai Z, Yu X, Zhang H, Kim T, Braun PV, et al. Micromechanical devices with controllable stiffness fabricated from regular 3D porous materials. J Micromech Microeng. 2014, 24(10):105006.
28. Zakhidov AA, Baughman RH, Iqbal Z, Cui C, Khayrullin I, Dantas SO, et al. Carbon structures with three-dimensional periodicity at optical wavelengths. Science. 1998, 282(5390): 897–901.
29. Blanco A, Chomski E, Grabtchak S, Ibisate M, John S, Leonard SW, et al. Large-scale synthesis of a silicon photonic crystal with a complete three-dimensional bandgap near 1.5 micrometres. Nature. 2000, 405(6785):437–40.
30. Lee HS, Kubrin R, Zierold R, Petrov AY, Nielsch K, Schneider GA, et al. Photonic properties of titania inverse opal heterostructures. Opt Mater Express. 2013, 3(8):1007.
31. Kubrin R, Lee HS, Zierold R, Petrov AY, Janssen R, Nielsch K, et al. Stacking of ceramic inverse opals with different lattice constants. J Am Chem Soc. 2012, 95(7):2226–35.
32. Kubrin R, Lee HS, Petrov A, Janssen R, Schneider GA, Bachmann J, et al. Towards ceramic 3DOM-materials as novel high-temperature reflective coatings and filters for thermophotovoltaics. IOP Conf Ser: Mater Sci Eng. 2011, 18(18):182004.
33. Bueno P, Furlan KP, Hotza D, Janssen R. High-temperature stable inverse opal photonic crystals via mullite-sol-gel infiltration of direct photonic crystals. J Am Chem Soc. 2018, 24(5): 13146.
34. Campos HG, Furlan KP, Garcia DE, Blick R, Zierold R, Eich M, et al. Effects of processing parameters on 3D structural ordering and optical properties of inverse opal photonic crystals produced by atomic layer deposition. Int J Cer Eng Sci. 2019, 1(2): 68–76.
35. Furlan KP, Pasquarelli RM, Krekeler T, Ritter M, Zierold R, Nielsch K, et al. Highly porous α-Al_2O_3 ceramics obtained by sintering atomic layer deposited inverse opals. Ceram Int. 2017, 43(14):11260–4.
36. Holland BT. Synthesis of macroporous minerals with highly ordered three-dimensional arrays of spheroidal voids. Science. 1998, 281(5376):538–40.
37. do Rosário JJ, Berger JB, Lilleodden ET, McMeeking RM, Schneider GA. The stiffness and strength of metamaterials based on the inverse opal architecture. Extreme Mech Lett. 2017, 12:86–96.
38. Zhou J, Li H, Ye L, Liu J, Wang J, Zhao T, et al. Facile fabrication of tough SiC inverse opal photonic crystals. J Phys Chem C. 2010, 114(50):22303–8.
39. Kubrin R, Pasquarelli RM, Waleczek M, Lee HS, Zierold R, do Rosário JJ, et al. Bottom-up fabrication of multilayer stacks of 3D photonic crystals from titanium dioxide. ACS Appl Mater Interfaces. 2016, 8(16):10466–76.
40. Holland BT, Blanford CF, Do T, Stein A. Synthesis of highly ordered, three-dimensional, macroporous structures of amorphous or crystalline inorganic oxides, phosphates, and hybrid composites. Chem Mater. 1999, 11(3):795–805.
41. Sokolov S, Bell D, Stein A. Preparation and characterization of macroporous α-alumina. J Am Chem Soc. 2003, 86(9): 1481–6.
42. Waterhouse GIN, Chen W-T, Chan A, Jin H, Sun-Waterhouse D, Cowie BCC. Structural, optical, and catalytic support properties of γ-Al_2O_3 inverse opals. J Phys Chem C. 2015, 119(12): 6647–59.
43. do Rosário JJ, Häntsch Y, Pasquarelli RM, Dyachenko PN, Vriend E, Petrov AY, et al. Advancing the fabrication of YSZ-inverse photonic glasses for broadband omnidirectional reflector films. J Eur Ceram Soc. 2019, 39(11):3353–63.
44. Bauer J, Schroer A, Schwaiger R, Kraft O. Approaching theoretical strength in glassy carbon nanolattices. Nat Mater. 2016, 15(4):438–43.
45. Roa JJ, Coll A, Bermejo S, Jiménez-Piqué E, Alcubilla R, Castañer L, et al. Mechanical properties of Al_2O_3 inverse opals by means of nanoindentation. J Phys D: Appl Phys. 2016, 49(45):455303.
46. Galisteo-López JF, Ibisate M, Sapienza R, Froufe-Pérez LS, Blanco A, López C. Self-assembled photonic structures. Adv Mater Weinheim. 2011, 23(1):30–69.
47. King JS, Graugnard E, Summers CJ. TiO_2 inverse opals fabricated using low-temperature atomic layer deposition. Adv Mater Weinheim. 2005, 17(8):1010.
48. Vogel N, Retsch M, Fustin C-A, Del Campo A, Jonas U. Advances in colloidal assembly: the design of structure and hierarchy in two and three dimensions. Chem Rev. 2015, 115(13):6265–311.
49. Norris DJ, Arlinghaus EG, Meng L, Heiny R, Scriven LE. Opaline photonic crystals: how does self-assembly work? Adv Mater Weinheim. 2004, 16(16):1393–9.
50. King JS, Neff CW, Summers CJ, Park W, Blomquist S, Forsythe E, et al. High-filling-fraction inverted ZnS opals fabricated by

atomic layer deposition. Appl Phys Lett. 2003, 83(13):2566–8.
51. Hong TL, Liu HT, Yeh CT, Chen SH, Sheu FC, Leu LJ, et al. Electron microscopic studies on pore structure of alumina. Appl Catal, A. 1997, 158(1-2):257–71.
52. Zaman AC, Üstündağ CB, Kaya C. Boehmite derived surface functionalized carbon nanotube-reinforced macroporous alumina ceramics. J Eur Ceram Soc. 2010, 30(12):2525–31.
53. Barmala M, Moheb A, Emadi R. Applying Taguchi method for optimization of the synthesis condition of nano-porous alumina membrane by slip casting method. J Alloys Compd. 2009, 485(1–2):778–82.
54. Dutta S, Kim TB, Krentz T, Vinci RP, Chan HM. Sol–gel-derived single-crystal alumina coatings with vermicular structure. J Am Chem Soc. 2011, 94(2):340–3.
55. Wang L, Hu J, Cheng Y, Fu Z, Shen Z, Xiong Y. Defect formation by order coalescence in vermicular grains during alumina phase transformation. Scr Mater. 2015, 107:59–62.
56. Yadlovker D, Berger S. Nucleation and growth of single crystals with uniform crystallographic orientation inside alumina nanopores. J Appl Phys. 2007, 101(3):34304.
57. Richerson DW. Modern ceramic engineering: Properties, processing, and use in design. 2nd ed. New York, NY: M. Dekker; 1992.
58. Abaqus 3DEXPERIENCE. Johnston, RI, USA: Dassault Systemes SIMULIA Corp; 2020.

SUPPORTING INFORMATION

Additional supporting information can be found online in the Supporting Information section at the end of this article.

How to cite this article: Gomez-Gomez A, Winhard B, Lilleodden E, Huber N, Furlan KP. Unraveling the role of shell thickness and pore size on the mechanical properties of ceramic-based macroporous structures. J Am Ceram Soc. 2023;106:1273–1286.
https://doi.org/10.1111/jace.18811